



AMERICAN METEOROLOGICAL SOCIETY

Monthly Weather Review

EARLY ONLINE RELEASE

This is a preliminary PDF of the author-produced manuscript that has been peer-reviewed and accepted for publication. Since it is being posted so soon after acceptance, it has not yet been copyedited, formatted, or processed by AMS Publications. This preliminary version of the manuscript may be downloaded, distributed, and cited, but please be aware that there will be visual differences and possibly some content differences between this version and the final published version.

The DOI for this manuscript is doi: 10.1175/MWR-D-16-0214.1

The final published version of this manuscript will replace the preliminary version at the above DOI once it is available.

If you would like to cite this EOR in a separate work, please use the following full citation:

Dörnbrack, A., S. Gisinger, M. Pitts, L. Poole, and M. Maturilli, 2016: Multilevel cloud structures over Svalbard. *Mon. Wea. Rev.* doi:10.1175/MWR-D-16-0214.1, in press.

© 2016 American Meteorological Society



Multilevel cloud structures over Svalbard

Andreas Dörnbrack¹ and Sonja Gisinger

Institut für Physik der Atmosphäre, DLR Oberpfaffenhofen, Germany

Michael C. Pitts

NASA Langley Research Center, Hampton, Virginia 23681 USA

Lamont R. Poole

Science Systems and Applications, Incorporated, Hampton, Virginia 23666 USA

Marion Maturilli

Alfred Wegener Institute, Helmholtz Centre for Polar and Marine Research,

Telegrafenberg A43, D-14473 Potsdam

Corresponding author: Andreas Dörnbrack, DLR Oberpfaffenhofen, Institut für Physik der Atmosphäre,

Münchener Str. 20, D – 82234 Wessling, Germany, Email: andreas.doernbrack@dlr.de

24 **Abstract**

25

26 The presented picture of the month is a superposition of space-borne lidar observations and high-
27 resolution temperature fields of the ECMWF integrated forecast system (IFS). It displays
28 complex tropospheric and stratospheric clouds in the Arctic winter 2015/16. Near the end of
29 December 2015, the unusual northeastward propagation of warm and humid subtropical air
30 masses as far north as 80°N lifted the tropopause by more than 3 km in 24 h and cooled the
31 stratosphere on a large scale. A widespread formation of thick cirrus clouds near the tropopause
32 and of synoptic-scale polar stratospheric clouds (PSCs) occurred as the temperature dropped
33 below the thresholds for the existence of cloud particles. Additionally, mountain waves were
34 excited by the strong flow at the western edge of the ridge across Svalbard, leading to the
35 formation of mesoscale ice PSCs. The most recent IFS cycle using a horizontal resolution of 8
36 km globally reproduces the large-scale and mesoscale flow features and leads to a remarkable
37 agreement with the wave structure revealed by the space-borne observations.

38 **1 Introduction**

39 The “picture of the month” as presented in this short contribution is not a photo of the sky
40 spontaneously shot from a digital camera. The picture as displayed in Figure 1 is a combination
41 of space-borne measurements by the CALIOP (Cloud-Aerosol Lidar with Orthogonal
42 Polarization) instrument onboard the CALIPSO (Cloud-Aerosol Lidar and Infrared Pathfinder
43 Satellite Observations) satellite during one of several Arctic overpasses on 30 December 2015
44 and a high-resolution short-term forecast of a numerical weather prediction (NWP) model
45 utilizing an unprecedented global resolution of about 8 km (for data sources, see Appendix). In
46 our days of ceaseless swells of pictures taken everywhere and anytime on the planet, a snapshot
47 taken from a sensor much different than a camera, taken from a perspective so much different
48 than from Earth, and superimposed with numerical predictions reflecting the observed flow
49 features with a remarkable realism elicits wonder and admiration.

50 The selected “picture of the month” displays tropospheric and stratospheric cloud structures
51 which appeared simultaneously during a remarkable meteorological situation in the high Arctic
52 near Svalbard on 30 December 2015. The resulting spectacular and uncommon appearance of
53 diverse cloud types and structures at different layers reaching up to 28 km altitude was
54 documented by the CALIOP measurements of total attenuated backscatter at 532 nm (Fig. 1a).
55 The CALIOP observations show an extensive, elongated structure of cirrus clouds within the
56 upper troposphere up to an altitude of about 13 km. The cirrus clouds are also nicely seen in the
57 infrared satellite image at this time (Fig. 2). Slightly more than 6 km above this cirrus deck,
58 CALIOP detected a nearly 8 km deep layer of synoptic-scale polar stratospheric clouds (PSCs)
59 embedded in an extended cold layer with temperatures less than 191 K. Within this layer,
60 vertically tilted and horizontally separated patterns of enhanced attenuated backscatter are
61 collocated with cold stratospheric temperature values less than 185 K (Fig. 1b). They are

62 reminiscent of mountain-wave induced PSCs (e.g. Maturilli and Dörnbrack, 2006, Fig. 9). This
63 first, qualitative interpretation is supported by the very structured ice PSCs occurring in a region
64 both above and downstream of Svalbard's mountains and above the underlying clouds near the
65 tropopause as mentioned above. As shown later, the satellite trace as sketched in Figs. 3 and 6
66 was nearly parallel to the stratospheric winds at this time and the mountain-wave induced
67 temperature anomalies are tilted into the ambient wind.

68 The spectacular display of PSCs¹ has fascinated people for a long time and they have been
69 observed scientifically since the 1880s (e.g. Backhouse, 1885, Geelmuyden, 1885, Mohn, 1893,
70 Stanford and Davies, 1974). A first step to explain the nature of these clouds was the exact
71 determination of their height range between 20 and 30 km by Störmer (1929, 1931). During the
72 recent thirty years, PSCs were systematically monitored because chemical reactions on cloud
73 particles play a major part in the depletion of the ozone layer (Solomon, 1999). The reactions are
74 very efficient at low temperatures due to the increase in particle surface area and in
75 heterogeneous reaction rates (Peter, 1997). The large interannual variability of the Arctic polar
76 vortex and of the polar cap minimum temperatures attained during northern hemispheric winters
77 (Fig. 3) regularly sparks off the scientific interest about the possible formation of PSCs and the
78 consequential ozone depletion in spring. For an overview of the evolution of the recent winter
79 2015/2016, see the excellent review by Manney and Lawrence (2016).

80 PSCs form in a variety of ways. First of all, the ambient stratospheric temperatures must
81 fall below a certain threshold where liquid or solid particles can form. Here, different freezing
82 processes (homogeneous and/or heterogeneous freezing) determine the composition of the PSC
83 particles. Generally, one differentiates between ice PSCs, which can exist at $T < T_{\text{FROST}}$, solid
84 nitric acid trihydrate (NAT) PSCs, which can exist at $T < T_{\text{NAT}} (\approx T_{\text{FROST}} + 7 \text{ K})$, and liquid

¹ These clouds are often called mother-of-pearl clouds because of their magnificent display of spectral colors.

85 supercooled ternary solution (STS; $\text{HNO}_3/\text{H}_2\text{O}/\text{H}_2\text{SO}_4$) PSCs, which can exist at $T \lesssim T_{\text{FROST}} + 3$
86 K. Since T_{FROST} depends on atmospheric humidity it varies with altitude ($T_{\text{FROST}} \approx 188$ K at 50
87 hPa and $T_{\text{FROST}} \approx 185$ K at 30 hPa). PSCs can be observed in-situ by instruments flying on
88 balloons (e.g. Rosen et al., 1992) or by in-situ airborne sensors (e.g. Dye et al., 1996). The high
89 altitudes and vertical extent of PSCs favor remote-sensing systems such as lidars operated on
90 ground (e.g. di Liberto et al., 2014) or on aircraft (e.g. Browell et al., 1990), or satellite solar
91 occultation PSC measurements (e.g. Strawa et al., 2002). Most of the recent studies on PSCs
92 focused on the composition and sizes of the particles (e.g. Reichardt et al., 2015) and chemical
93 processes occurring at their surfaces that yield ozone-destructive, reactive chlorine species (e.g.
94 Solomon, 1999).

95 Numerical modelling of PSCs has always been a challenging task as chemical and
96 dynamical aspects of their formation and existence must be combined (e.g., Reichardt et al.,
97 2004). Their formation is primarily influenced by large-scale processes such as the radiative
98 cooling inside the Arctic polar vortex. Moreover, it is known that both synoptic-scale as well as
99 mesoscale weather systems influence the formation of PSCs and the associated chemical
100 reactions (Teitelbaum and Sadourny, 1998, Carslaw et al., 1998). Simulation of mesoscale
101 mountain waves especially posed a challenge, and special methods such as linear wave prediction
102 models and mesoscale forecast models were used in the past to predict their local formation (e.g.,
103 Dörnbrack et al., 1998, Eckermann et al., 2006). In this day and age, global operational NWP
104 models use spatial resolutions which hardly could be attained by limited area models several
105 years ago. For example, the European Centre for Medium-Range Weather Forecasts (ECMWF)
106 currently runs its operational predictions of the Integrated Forecast System (IFS) cycle 41r2 at 8
107 km globally (Hólm, et al, 2016, Malardel and Wedi, 2016). Here, it will be shown that the
108 conditions under which the observed mesoscale ice PSCs formed can be resolved by the IFS.

109

110 **2. Weather Situation and Gravity Wave Characteristics**

111 *Cold Arctic Polar Vortex*

112 The composite “picture of the month” was taken in a period when the temperatures inside
113 the Arctic stratospheric vortex were unusually cold (Fig. 3). In November/December 2015, the
114 Arctic vortex was minimally disturbed by upward propagating planetary waves (Matthias et al.,
115 2016) and the polar cap minimum temperature T_{MIN} between 65°N and 90°N dropped well below
116 the climatological mean. The red T_{MIN} -line in Fig. 3 reveals that the threshold of T_{NAT} at 50 hPa
117 was already reached at the beginning of December 2015, and T_{MIN} dropped below T_{FROST} at the
118 end of 2015. Apparently, the minimum temperatures falling below T_{FROST} at the end of the year
119 constitute a new record. In its further evolution, the Arctic polar vortex remained cold, stable and
120 coherent until end of February 2016 (Manney and Lawrence, 2016). The final warming already
121 occurred at the beginning of March 2016. Such an early collapse of the cold polar vortex is in
122 accordance with the findings of the climatological study of Hu et al. (2014). In such a cold
123 stratospheric environment, the period of temperatures below T_{FROST} and T_{NAT} at 50 hPa lasted
124 more than one month and three months, respectively. CALIPSO observations until the end of
125 January 2016 confirm the widespread occurrence of PSCs in the Arctic.

126 *Tropospheric Flow Conditions*

127 Near the end of December 2015, the tropospheric flow over the Northern Atlantic was
128 characterized by an anticyclonic Rossby wave breaking event. Figure 4 illustrates the late stages
129 of this event by means of the height and wind at the 2 PVU surface from the ECMWF operational
130 analyses valid on 29 December 2015 at 18 UTC and twelve hours later on 30 December 2015 at
131 06 UTC, respectively. A ridge with tropopause heights of up to 13 km extended north to latitudes

132 above 80°N. Between this ridge with high surface pressure (maximum at about 1038 hPa) over
133 Eastern Europe and a surface pressure low over Greenland (minimum at about 968 hPa), a strong
134 south-westerly low-level flow extended over the entire northern Atlantic and the Norwegian Sea
135 towards Svalbard (Fig. 5 a, b). East of Greenland, warm and moist air was advected northwards
136 as shown by the increased values of the equivalent potential temperature (Fig. 5 c, d). Further
137 south near Iceland, a storm with a core pressure of 930 hPa on 30 December 2015 at 06 UTC
138 propagated north. This weather situation led to a combination of two processes relevant for the
139 cloud structures as shown in Fig. 1. First, the increase of the tropopause height associated with
140 the anticyclonic Rossby wave breaking led to a cooling of the air masses in the upper troposphere
141 and lower stratosphere (UTLS) due to adiabatic expansion. Secondly, the strong troposphere-
142 deep pressure gradient between the upstream Greenland/Iceland cyclone complex and the
143 downstream Scandinavian ridge forced a strong flow across the mountains of Svalbard which
144 reached a maximum at 30 December 2015 at 00 UTC with horizontal winds larger 25 m s⁻¹ at 700
145 hPa (Fig. 5 e, f).

146 A series of five radiosonde ascents from Ny-Ålesund, Svalbard (79°N, 12°E) covering the
147 period from 27 to 31 December 2015 (Fig. 6) illustrates the previous findings from the IFS
148 analyses. First of all, the warming of the troposphere by about 15 K due to the warm-air
149 advection can be clearly seen in Fig. 6a. During the same period, the tropopause rose and
150 sharpened dramatically. Indeed, the vertical temperature profiles of 29 and 30 December 2015 at
151 12 UTC are more typical for a mid-latitude station than for an Arctic location.

152 *Large-scale cooling*

153 An analysis of radiosonde soundings from Ny-Ålesund, Svalbard reveals a drop of the
154 mean temperature between 10 and 13 km by about 9 K in three days reaching 200 K on 29

155 December (see Table 1). This strong cooling associated with the tropopause ascent led to the
156 formation of the observed cirrus clouds at these levels. Not only the temperature in the vicinity of
157 the tropopause dropped, but the mean stratospheric temperature between 20 and 25 km altitude
158 also decreased by about 4 K due to the lifting of the atmosphere above the ridge (Table 1). In this
159 way, the mean temperatures near 30 hPa dropped below 185 K, the ice existence temperature
160 T_{FROST} . However, increased backscatter values indicative of ice PSCs appear primarily at and
161 leeward of the wave crests as shown in Figure 1a. The adiabatic cooling by ascending air parcels
162 led to a local temperature decrease and to ice nucleation which require temperatures $T \lesssim T_{\text{FROST}} -$
163 4 K. Thus, we conclude that the stratospheric ice clouds as seen by CALIOP were generated due
164 to mountain-wave induced temperature anomalies.

165 *Mountain-wave induced cooling*

166 As documented in Table 1, the magnitude of stratospheric temperature fluctuations ΔT^{SP}
167 measured in the layer from 20 to 25 km increased from values of around 5 K on 26 December
168 2015 to values up to 12 K on 29 and 30 December 2015. These fluctuations are represented by
169 the wave-like temperature perturbations as shown in Fig. 1b. There, the areas of increased
170 backscatter nearly coincide with localized regions of $T < T_{\text{FROST}}$. It must be noted that the
171 CALIPSO satellite trace was nearly aligned with the stratospheric winds as indicated by the
172 orientation of the contour lines of the geopotential height in Fig. 7. Therefore, the ice PSCs as
173 well as the simulated mountain waves are tilted into the ambient stratospheric wind which is
174 oriented from west to east in Fig. 1. The tilting into the ambient wind is characteristic for upward
175 propagating mountain waves (Nappo, 2002).

176 Figure 7 depicts horizontal cross-sections of the stratospheric wave structure at 10 hPa and
177 30 hPa by means of the vertical velocity and the absolute temperature from IFS analyses. A

178 sequence of northwest-southeast oriented updraft-downdraft couplets extends from Svalbard
179 towards the northeast. Altogether, there are four stratospheric cold anomalies associated with the
180 adiabatic cooling in the mountain waves at 10 hPa (Fig. 7 a, c). Their positions clearly correspond
181 to the areas of $T < 185$ K and the CALIOP PSC observations as presented in Fig. 1b. At the lower
182 level of 30 hPa (Fig. 7 b, d), similarly oriented structures exist whereby the cold areas are slightly
183 shifted to the northeast in accordance with the tilt of the observed PSCs (Fig. 1).

184 *Gravity Wave Characteristics*

185 Mountain waves are generated and propagate into the stratosphere if there is a major flow
186 across the topography (low-level forcing), the tropospheric and stratospheric winds are large
187 enough to avoid the formation of wave-induced critical levels, and there is no significant turning
188 of the wind with altitude (e.g., Fritts et al. 2016). All these requirements were satisfied in the
189 Svalbard region for the period from 28 to 30 December 2015. The horizontal wind in the lower
190 troposphere (averaged from 2 to 5 km altitude) increased gradually from about 5 m s^{-1} to about 30
191 m s^{-1} in the period from 25 to 31 December 2015 as shown by the radiosonde data (Figure 8a).
192 Also near the tropopause level, the averaged wind in the UTLS increased markedly after 28
193 December up to values of 60 m/s and turned from westerly to southwesterly as the ridge
194 propagated over Svalbard (Table 1). Altogether, the directional shear between tropospheric and
195 stratospheric winds weakened in this period (Fig. 6c). The combination of strong winds in the
196 lower troposphere followed by increased mid- to upper tropospheric winds and the presence of
197 wind of about 25 m s^{-1} in altitudes above (15 to 25 km) created a favorable flow situation for
198 mountain wave excitation and vertical propagation to higher altitudes. Indeed, both the
199 temperature and wind profiles from the radiosonde soundings reveal wavelike structures in the
200 stratosphere (Fig. 6) which were analyzed to estimate the kinetic and potential energies of the

201 gravity waves as well as their intrinsic frequency and horizontal wavelength from the radiosonde
202 soundings.

203 For this purpose, a polynomial fit was applied to calculate background profiles of the
204 horizontal wind components and the potential temperature from the radiosonde profiles between
205 15 and 25 km altitude. The perturbations calculated as difference between the background
206 profiles and the actual radiosonde profiles were treated as signatures of internal gravity waves
207 from which the kinetic and potential energies are determined according to Murphy et al. (2014).
208 Figure 8b shows a peak in the stratospheric kinetic and potential energy densities at 30 December
209 2015. This enhancement as well as the localized wave appearance over and in the lee of Svalbard
210 (Fig. 7) indicate that the waves are generated by the flow over the mountains. Stokes analysis of
211 the velocity perturbations (Eckermann and Vincent, 1989) of the 30 December radio sounding
212 revealed the intrinsic frequency Ω of the dominant gravity wave mode being $6.7 f$, where f is the
213 Coriolis parameter. Assuming that the dominant gravity wave mode is a stationary mountain
214 wave its horizontal wavelength can be calculated using the relationship between Ω , horizontal
215 wavenumber k and the background wind U for stationary waves $\Omega = -k U$, i.e. (Nappo, 2002).
216 Having a background wind of 25 to 35 m s^{-1} (Fig. 8a) the determined horizontal wavelength is
217 approximately 180 ... 250 km. The effect of the Coriolis force alters the dispersion relationship
218 of non-rotating hydrostatic gravity waves and allows a slantwise, e.g. horizontal and vertical,
219 propagation (Gill 1980, Chapter 8). This explains the multiple mountain-wave induced
220 temperature anomalies separated by about 180 km (Fig. 1b and Fig. 7d). Another example of a
221 similar stratospheric cloud structure above Scandinavia and a more detailed discussion can be
222 found in Dörnbrack et al. (2002).

223 The effect of mesoscale temperature fluctuations on the polar cap minimum temperatures T_{MIN} at
224 50 hPa is illustrated by the new IFS cycle 41r2. Figure 3 contains two T_{MIN} curves for a period of
225 3 months when the new IFS cycle was not yet operational. The red line depicts the former IFS
226 cycle 41r1 with 16 km horizontal resolution and the shorter black line is T_{MIN} of the new, updated
227 operational cycle 41r2 with 8 km horizontal resolution. After 8 March 2016, IFS cycle 41r2
228 became operational and continues as red line. Obviously, the higher resolution IFS run achieved
229 much lower T_{MIN} in certain periods, especially at the end of December 2015 and at the end of
230 January 2016 when deviations of up to 7 K occurred. These stratospheric temperature minima
231 were primarily generated by mesoscale gravity waves at various places in the Arctic, especially
232 over Greenland and Scandinavia as shown in Fig. 9 for December 2015. Gravity wave activity
233 was identified by values of the horizontal divergence being larger than $2 \cdot 10^{-4} \text{ s}^{-1}$ as suggested by
234 Dörnbrack et al. (2012) and Khaykin et al. (2015).

235

236 **4. Conclusions**

237 The uniqueness of this contribution to the “picture of the month” is not only justified by the
238 unusual meteorological situation in the Arctic in mid-winter, but also by the co-existence of
239 tropospheric clouds, i.e. cirrus clouds attached to a 12 km high and sharp tropopause, and
240 different types of PSCs between 18 km and 28 km altitude over a limited area poleward of 80°N .
241 Synoptic-scale lifting was responsible for formation of the ice clouds near the tropopause and
242 NAT or STS PSCs in the stratosphere. The total large-scale ascent was also associated with the
243 formation of an ozone mini-hole observed by OMI² which was generally aligned with the
244 tropospheric ridge as shown in Fig. 3, see e.g. Peters et al. (1995) for dynamical aspects of ozone
245 mini-hole formation. Adiabatic cooling in the ascending branches of mesoscale mountain waves

² http://ozonewatch.gsfc.nasa.gov/Scripts/big_image.php?date=2015-12-31&hem=N

246 dropped the stratospheric temperatures far below the threshold temperature for the existence of
247 ice PSCs. The simultaneous formation of synoptic and mesoscale PSCs inside the Arctic
248 stratospheric vortex happened during a rare meteorological situation during the Northern
249 Hemisphere mid-winter. Moreover, it is the remarkable agreement of the simulated wave
250 structure in the IFS short-term forecast and the space-borne observations which indicates a
251 significant trend that the finer resolution and increasing realism of operational NWP model
252 outputs offers a valuable quantitative source for mesoscale flow components which were hitherto
253 not accessible globally (Bauer et al., 2015).

254

255 **Appendix**

256 *Numerical weather prediction model data*

257 Operational analyses of the integrated forecast system (IFS) of the European Centre for Medium-
258 Range Weather Forecasts (ECMWF) are used to provide meteorological data to characterize the
259 atmospheric situation. The operational analyses and forecasts of the deterministic high-resolution
260 (HRES) IFS cycle 41r2 have a horizontal resolution of about 8 km (T_C1279) and 137 vertical
261 levels ($L137$)³. The model top is located at 0.01 hPa. The enhanced horizontal resolution was
262 achieved by changing from linear (T_L) to cubic (T_C) spectral truncation and introducing an
263 octahedral reduced Gaussian grid. With the cubic spectral truncation the shortest resolved wave is
264 represented by four rather than two grid points and the octahedral grid is globally more uniform
265 than the previously used reduced Gaussian grid (Malardel and Wedi, 2016). In December 2015,
266 the IFS cycle 41r2 was not yet in its operational mode but products were disseminated among the
267 users. So, we were able to retrieve forecasts and analysis fields for the current contribution.

³ <https://software.ecmwf.int/wiki/display/FCST/Implementation+of+IFS+cycle+41r2> and
<http://www.ecmwf.int/en/about/media-centre/news/2016/new-forecast-model-cycle-brings-highest-ever-resolution>

268 *CALIPSO data*

269 The primary instrument on CALIPSO is a lidar (CALIOP, or Cloud-Aerosol Lidar with
270 Orthogonal Polarization) that measures backscatter at wavelengths of 1064 nm and 532 nm, with
271 the 532-nm signal separated into orthogonal polarization components parallel and perpendicular
272 to the polarization plane of the outgoing laser beam. A description of CALIOP and its on-orbit
273 performance can be found in Hunt et al. (2009), and details on calibration of the CALIOP data
274 are provided by Powell et al. (2009). CALIOP has proven to be an excellent system for observing
275 PSCs (Pitts et al., 2007; 2009; 2011; 2013).

276

277 **Acknowledgements**

278 Part of this research was funded by the German research initiative “Role of the Middle
279 Atmosphere in Climate (ROMIC)” funded by the German Ministry of Research and Education in
280 the project “Investigation of the life cycle of gravity waves (GW-LCYCLE)”. The research of
281 Sonja Gisinger was supported by the research group “Multiscale dynamics of gravity waves (MS-
282 GWaves)” in the project “Modification of gravity waves propagating across the tropopause”.
283 Access to the ECMWF data was possible through the special project “HALO Mission Support
284 System”. The presented radiosonde data were obtained at the AWIPEV research base at Ny-
285 Ålesund, Svalbard. They are part of the Global Climate Observing Systems (GCOS) Reference
286 Upper-Air Network (GRUAN), available via the webpage www.gruan.org. The very constructive
287 comments of three anonymous reviewers helped considerably to improve the paper.

288 **References**

289 Backhouse, W., 1885: Iridescent clouds, *Nature*, **31**, 192–193.

290
291 Bauer P, A. Thorpe, and G. Brunet, 2015: The quiet revolution of numerical weather prediction.
292 *Nature*, **525**(7567): 47–55.

293
294 Browell, E. V. , C. F. Butler, S. Ismail, P. A. Robinette, A. F. Carter, N. S. Higdon, O. B. Toon,
295 M. R. Schoeberl, and A. F. Tuck, 1990: Airborne lidar observations in the wintertime Arctic
296 stratosphere: polar stratospheric clouds, *Geophys. Res. Lett.*, **17**, 385–388.

297
298 Carslaw, K. S., and Coauthors, 1998: Increased stratospheric ozone depletion due to mountain-
299 induced atmospheric waves. *Nature*, **391**, 675–678.

300
301 Dee, D., and Coauthors, 2011: The ERA-Interim reanalysis: Configuration and performance of
302 the data assimilation system. *Quart. J. Roy. Meteor. Soc.*, **137**, 553–597.

303
304 Dörnbrack, A., M. Leutbecher, H. Volkert, and M. Wirth, 1998: Mesoscale forecasts of
305 stratospheric mountain waves. *Meteor. Appl.*, **5**, 117–126.

306
307 Dörnbrack, A., T. Birner, A. Fix, H. Flentje, A. Meister, H. Schmid, E. V. Browell, and M. J.
308 Mahoney, 2002: Evidence for inertia gravity waves forming polar stratospheric clouds over
309 Scandinavia. *J. Geophys. Res.* 107(D20), 8287, doi:10.1029/2001 JD000452.

310

311 Dörnbrack, A., Pitts, M. C., Poole, L. R., Orsolini, Y. J., Nishii, K., and Nakamura, H., 2012: The
312 2009–2010 Arctic stratospheric winter – general evolution, mountain waves and predictability of
313 an operational weather forecast model, *Atmos. Chem. Phys.*, **12**, 3659–3675, doi:10.5194/acp-12-
314 3659-2012.

315

316 Dye, J. E., D. Baumgardner, B. W. Gandrud, K. Drdla, K. S. Barr, D. W. Fahey, L. A. DelNegro,
317 A. Tabazadeh, H. H. Jonsson, J. C. Wilson, M. Loewenstein, J. R. Pdolske, and K. R. Chan,
318 1996: In-situ observations of an Antarctic polar stratospheric cloud: Similarities with Arctic
319 observations. *Geophysical Research Letters*, **23**, 1913–1916, DOI: 10.1029/96GL01812.

320

321 Eckermann, S. D. and R. A. Vincent, 1989: Falling sphere observations of anisotropic gravity
322 wave motions in the upper stratosphere over Australia. *Pure Appl. Geophys.*, **130**, 509–532.

323

324 Eckermann, S. D., A. Dörnbrack, H. Flentje, S. B. Vosper, M. J. Mahoney, T. P. Bui, and K. S.
325 Carslaw, 2006: Mountain Wave–Induced Polar Stratospheric Cloud Forecasts for Aircraft
326 Science Flights during SOLVE/THESEO 2000. *Wea. Forecasting*, **21**, 42–68. doi:
327 [10.1175/WAF901.1](https://doi.org/10.1175/WAF901.1)

328 Fritts, D. C., R. B. Smith, M. J. Taylor, J. D. Doyle, S. D. Eckermann, A. Dörnbrack, M. Rapp,
329 B. P. Williams, P.-D. Pautet, K. Bossert, N. R. Criddle, C. A. Reynolds, P. A. Reinecke, M.
330 Uddstrom, M. J. Revell, R. Turner, B. Kaifler, J. S. Wagner, T. Mixa, C. G. Kruse, A. D. Nugent,
331 C. D. Watson, S. Gisinger, S. M. Smith, R. S. Lieberman, B. Laughman, J. J. Moore, W. O.
332 Brown, J. A. Haggerty, A. Rockwell, G. J. Stossmeister, S. F. Williams, G. Hernandez, D. J.
333 Murphy, A. R. Klekociuk, I. M. Reid, and J. Ma, 2016: The Deep Propagating Gravity Wave
334 Experiment (DEEPWAVE): An Airborne and Ground-Based Exploration of Gravity Wave

335 Propagation and Effects from their Sources throughout the Lower and Middle Atmosphere, *Bull.*
336 *Am. Meteorol. Soc.*, **97**, 425–453 doi:10.1175/BAMS-D-14-00269.1.

337

338 Geelmuyden, H, 1885: Iridescent clouds, *Nature* **31**, 264.

339

340 Gill, A. E., 1982: *Atmosphere-Ocean Dynamics*, Academic Press, 662 pp.

341

342 Hólm, E., R. Forbes, S. Lang, L. Magnusson, and S. Malardel, 2016: New model cycle brings
343 higher resolution, ECMWF Newsletter, Spring 2016, 14-19.
344 <http://www.ecmwf.int/sites/default/files/elibrary/2016/16299-newsletter-no147-spring-2016.pdf>

345

346

347 Hu, J., R. Ren, and H. Xu, 2014: Occurrence of winter stratospheric sudden warming events and
348 the seasonal timing of spring stratospheric final warming, *J. Atmos. Sci.*, **71**, 2319–2334, doi:
349 10.1175/JAS-D-13-0349.1.

350

351 Khaykin, S. M., A. Hauchecorne, N. Mzé, and P. Keckhut, 2015: Seasonal variation of gravity
352 wave activity at midlatitudes from 7 years of COSMIC GPS and Rayleigh lidar temperature
353 observations, *Geophys. Res. Lett.*, **42**, 1251–1258, doi:10.1002/2014GL062891.

354

355 Di Liberto, L., F. Cairo, F. Fierli, G. Di Donfrancesco, M. Viterbini, T. Deshler, and M. Snels,
356 2014: Observation of Polar Stratospheric Clouds Over McMurdo (77.85°S, 166.67°E) (2006-
357 2010). *J. Geophys. Res.*, **119**, 5528–5541.

358

359 Liu, Z., M. A. Vaughan, D. M. Winker, C. A. Hostetler, L. R. Poole, D. Hlavka, W. Hart, and M.
360 McGill, 2004: Use of probability distribution functions for discriminating between cloud and
361 aerosol in lidar backscatter data. *J. Geophys. Res.*, **109**, D15202, doi:10.1029/2004JD004732.

362
363 Malardel, S. and N. P. Wedi, 2016: How does subgrid-scale parametrization influence nonlinear
364 spectral energy fluxes in global NWP models?, *J. Geophys. Res.*, **121**,
365 doi:10.1002/2015JD023970.

366
367 Manney, G. L. and Z. D. Lawrence, 2016: The major stratospheric final warming in 2016:
368 Dispersal of vortex air and termination of Arctic chemical ozone loss, *Atmos. Chem. Phys.*
369 *Discuss.*, doi:10.5194/acp-2016-633, in review.

370
371 Matthias, V., A. Dörnbrack, and G. Stober, 2016: The extraordinarily strong and cold polar
372 vortex in the early northern winter 2015/16. *Geophys. Res. Lett.*, under review.

373
374 Maturilli, M. and A. Dörnbrack, 2006: Polar stratospheric ice cloud above Spitsbergen, *J.*
375 *Geophys. Res.* **111**, D18, D18210, doi:10.1029/2005JD006967.

376
377 Mohn, H., 1893: Irisirende Wolken, *Meteorol. Z.*, **11**, 81–97.

378
379 Murphy, D. J., S. P. Alexander, A. R. Klekociuk, P. T. Love, and R. A. Vincent, 2014:
380 Radiosonde observations of gravity waves in the lower stratosphere over Davis, Antarctica. *J.*
381 *Geophys. Res.*, **119**, 11973–11996, doi:10.1002/2014JD022448.

382

383 Nappo, C. J., 2012: *An Introduction to Atmospheric Gravity Waves*, 2nd Edition, Academic Press,
384 400 pp.

385
386 Peter, T. 1997: Microphysics and heterogeneous chemistry of polar stratospheric clouds. *Annu.*
387 *Rev. Phys. Chem.*, **48**, 785–822.

388
389 Peters, D., J. Egger, and G. Entzian, 1995: Dynamical aspects of ozone mini-hole formation.
390 *Meteor. Atmos. Phys.*, **55**, 205–214.

391
392 Pitts, M. C., L. W. Thomason, L. R. Poole, and D. M. Winker, 2007: Characterization of polar
393 stratospheric clouds with spaceborne lidar: CALIPSO and the 2006 Antarctic season. *Atmos.*
394 *Chem. Phys.*, **7**, 5207–5228.

395
396 Pitts, M. C., L. R. Poole, and L. W. Thomason, 2009: CALIPSO polar stratospheric cloud obser-
397 vations: second-generation detection algorithm and composition discrimination. *Atmos. Chem.*
398 *Phys.*, **9**, 7577–7589.

399
400 Pitts, M. C., L. R. Poole, A. Dörnbrack, and L. W. Thomason, 2011: The 2009-2010 Arctic Polar
401 Stratospheric Cloud Season: A CALIPSO Perspective. *Atmos. Chem. Phys.*, **11**, 2161–2177.

402
403 Reichardt, J., A. Dörnbrack, S. Reichardt, P. Yang, and T. J. McGee, 2004: Mountain wave PSC
404 dynamics and microphysics from ground-based lidar measurements and meteorological
405 modeling. *Atmos. Chem. Phys.*, **4**, 1149–1165

406

407 Reichardt, J., S. Reichardt, C. Hostetler, P. Lucker, T. McGee, L. Twigg, A. Dörnbrack, M.
408 Schoeberl, and P. Yang, 2015: Mother-of-pearl cloud particle size and composition from aircraft-
409 based photography of coloration and lidar measurements. *Appl. Opt.*, **54**, B140–B153.
410

411 Rosen, J. M., N. T. Kjöme, V. U. Khattatov, V. V. Rudakov, and V. A. Yushkov, 1992:
412 Observations of ozone and polar stratospheric clouds at Heiss Island during winter 1988–1989. *J.*
413 *Geophys. Res.*, **97**, 8099–8104, doi:[10.1029/91JD02524](https://doi.org/10.1029/91JD02524).
414

415 Solomon, S., 1999: Stratospheric ozone depletion: a review of concepts and history. *Rev.*
416 *Geophys.* **37**, 275–316.
417

418 Stanford, J. L. and J. S. Davies, 1974: A century of stratospheric cloud reports: 1870–1972. *Bull.*
419 *Am. Meteorol. Soc.*, **55**, 213–219.
420

421 Störmer, C. 1929: Remarkable clouds at high altitudes. *Nature*, **123**, 940–941.
422

423 Störmer, C. 1931: Höhe und Farbverteilung der Perlmutterwolken. *Geofysiske Publikasjoner* **IX**,
424 3–25.
425

426 Strawa, A. W., K. Drdla, M. Fromm, R. F. Pueschel, K. W. Hoppel, E. V. Browell, P. Hamill,
427 and D. P. Dempsey, 2002: Discriminating Types Ia and Ib polar stratospheric clouds in POAM
428 satellite data. *J. Geophys. Res.*, **107**, 8291, doi:10.1029/2001JD000458.
429

430 Teitelbaum, H. and R. Sadourny, 1998: The role of planetary waves in the formation of polar
431 stratospheric clouds. *Tellus A*, **50**, 302–312.

432 **Tables**

433

Date	T^{TP} / K	$V_{\text{H}}^{\text{TP}} / \text{m s}^{-1}$	$\alpha^{\text{TP}} / \text{K}$	T^{SP} / K	$\Delta T^{\text{SP}} / \text{K}$
26 Dec 2015	209.3	8.7	254	188.8	4.7
27 Dec 2015	209.6	27.7	296	187.4	6.5
28 Dec 2015	205.9	23.3	268	187.3	8.4
29 Dec 2015	200.0	23.6	240	184.4	12.0
30 Dec 2015	204.7	36.8	241	185.4	10.1
31 Dec 2015	204.1	59.8	199	183.9	6.8

434

435 **Table 1:** Mean quantities in the UTLS averaged from 10 to 13 km altitude: absolute temperature
436 T^{TP} , horizontal wind V_{H}^{TP} , and wind direction α^{TP} from the radiosonde soundings in Ny-Ålesund.
437 The mean stratospheric temperature T^{SP} is averaged from 20 to 25 km altitude and ΔT^{SP} is the
438 difference between the measured maximum and minimum T in this layer.

439 **Figures**

440 **Figure 1:** Composite of 532 nm total attenuated backscatter ($10^{-3} \text{ km}^{-1} \text{ sr}^{-1}$, color shaded) from CALIOP
441 and ECMWF potential temperature (top, K, solid black lines) and absolute temperature (bottom, K, thin
442 black lines every 5 K and thick black lines at 185 K and 191 K) valid on 30 December 2015 at 04 UTC (+
443 4 h lead time from the 00 UTC HRES IFS forecast of cycle 41r2.

444 **Figure 2:** Thermal infra-red image (NOAA 19, channel 4: 10.3-11.3 μm) on 30 December 2015 0440 UTC
445 with the first third of the path of the CALIOP measurements (Fig. 1) as black arrow. Image provided by
446 NERC Satellite Receiving Station, Dundee University, Scotland (<http://www.sat.dundee.ac.uk>).

447 **Figure 3:** 6 hourly ECMWF reanalyses interim (ERA-Interim, Dee et al., 2011) data retrieved at a
448 horizontal resolution of 1° : Minimum temperature T_{MIN} (K) between 65°N to 90°N at the 50 hPa pressure
449 surface. Thick black line denotes the mean values of T_{MIN} averaged from 1979 – 2015, the shaded areas
450 encompass the minimum and maximum values of T_{MIN} attained at every date between 1979 and 2015.
451 The red line marks the evolution of T_{MIN} from operational analyses of the IFS cycle 41r1 until 8 March
452 2016. The thin black line indicates T_{MIN} from the IFS cycle 41r2 in the pre-operational phase 1 December
453 2015 until 8 March 2016 retrieved at a resolution of 0.125° . After 8 March 2016, the black line continues
454 as red curve of the operational IFS cycle 41r2.

455 **Figure 4:** Height of the dynamical tropopause (km, color shaded) and horizontal wind (m s^{-1} , barbs) at the
456 2 PVU surface on 29 December 2015 18 UTC (a) and 30 December 2015 06 UTC (b). The path of the
457 CALIPSO overpass is plotted as solid black line, the location of Ny-Ålesund, Svalbard is marked by a red
458 dot.

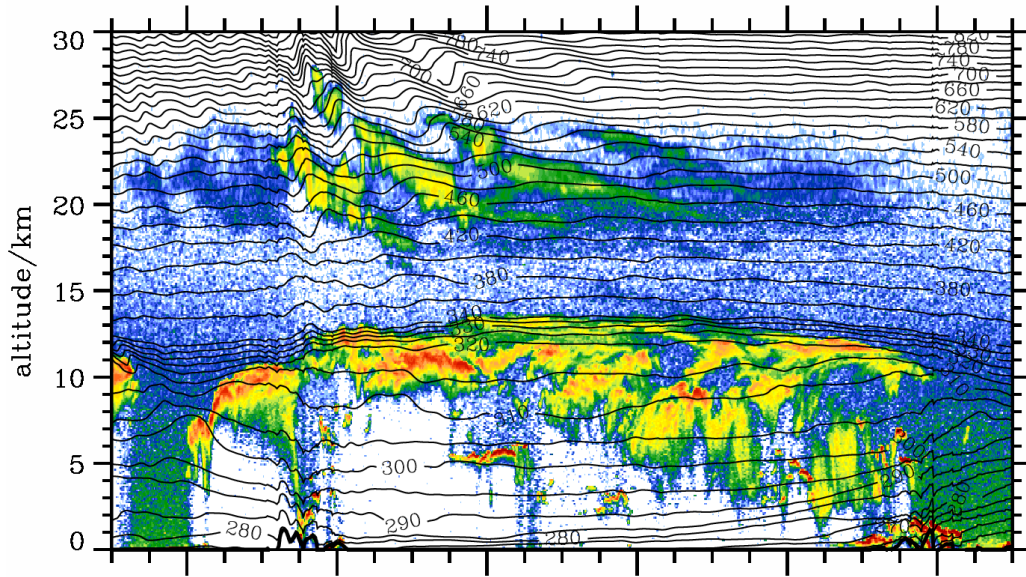
459 **Figure 5:** Tropospheric charts valid on 29 December 2015 18 UTC (left column) and 30 December 2015
460 06 UTC (right column). (a,b): Mean sea level pressure (hPa, contour lines), (c,d): Equivalent potential
461 temperature (K, color shaded) at 850 hPa, and (e,f): horizontal wind (m s^{-1} , color shaded) and geopotential
462 height (m, contour lines) at 700 hPa.

463 **Figure 6:** Vertical profiles of absolute temperature (a), horizontal wind (b), and wind direction (c) from
464 radiosonde launches in Ny-Ålesund, Svalbard on 27 December (black), 28 December (blue), 29 December
465 (thin red), 30 December (thick red), and 31 December (green) 2015 12 UTC, respectively.

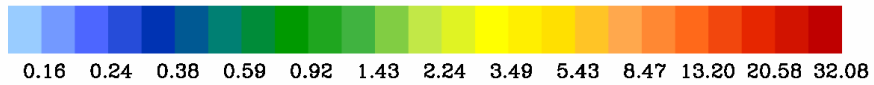
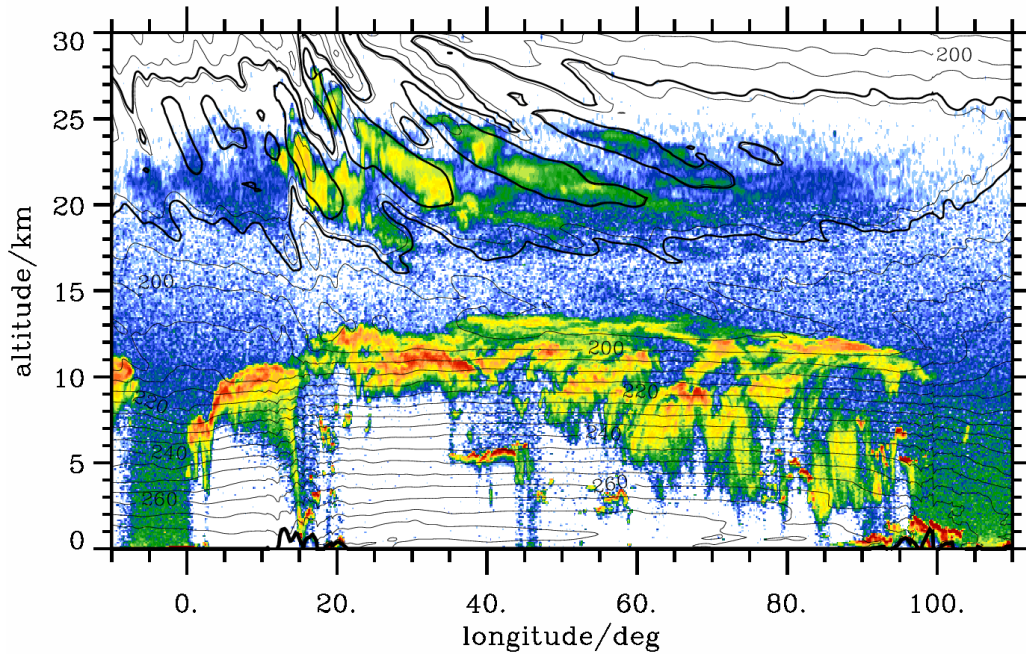
466 **Figure 7:** Vertical velocity (m s^{-1} , color shading, top row), absolute temperature (K, color shading, bottom
467 row), and geopotential height (m, black contour lines) from the IFS cycle 41r2 at 10 hPa (a, c) and at 30
468 hPa (b,d) valid on 30 December 2015 06 UTC. The path of the CALIPSO overpass is plotted as solid
469 black line, the location of Ny-Ålesund, Svalbard is marked by a red dot.

470 **Figure 8:** (a) Vertically averaged horizontal wind in the lower troposphere (2 to 5 km, red crosses), the
471 tropopause region (8 to 15 km, blue crosses), and in the stratosphere (15 to 25 km, black crosses). (b)
472 Stratospheric gravity wave kinetic and potential energies (red and blue crosses, respectively) determined
473 from the radiosonde soundings of Ny-Ålesund, Svalbard in an altitude range of 15 to 25 km.

474 **Figure 9:** Locations of the polar cap minimum temperatures T_{MIN} at 30 hPa (a) and 50 hPa (b) from 6
475 hourly ECMWF IFS cycle 41r2 analyses for December 2015. The red dots mark T_{MIN} -values where the
476 absolute value of the horizontal divergence is larger than $2 \cdot 10^{-4} \text{ s}^{-1}$. The large symbol is the location of
477 T_{MIN} on 30 December 2015 at 06 UTC.



478

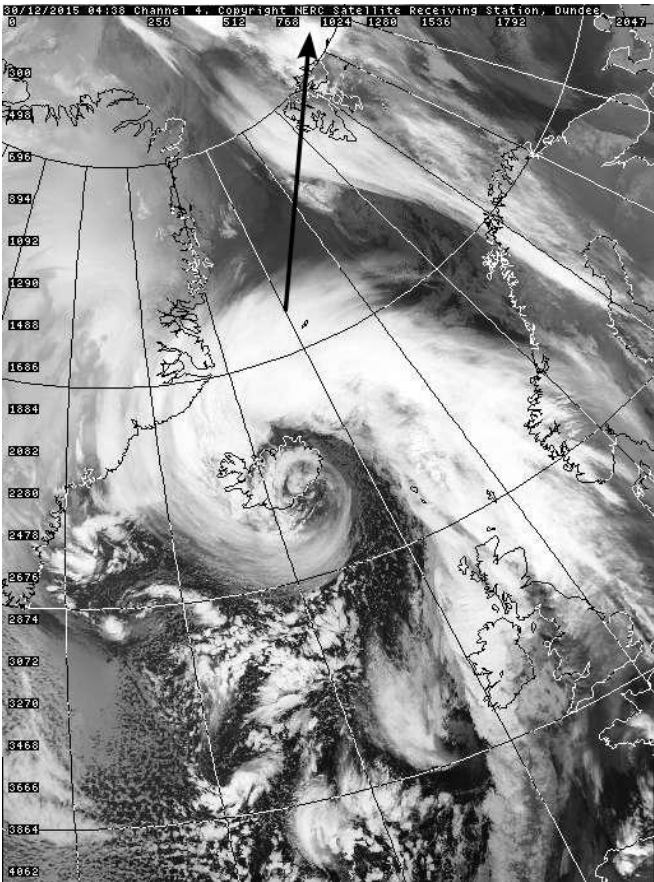


479

480

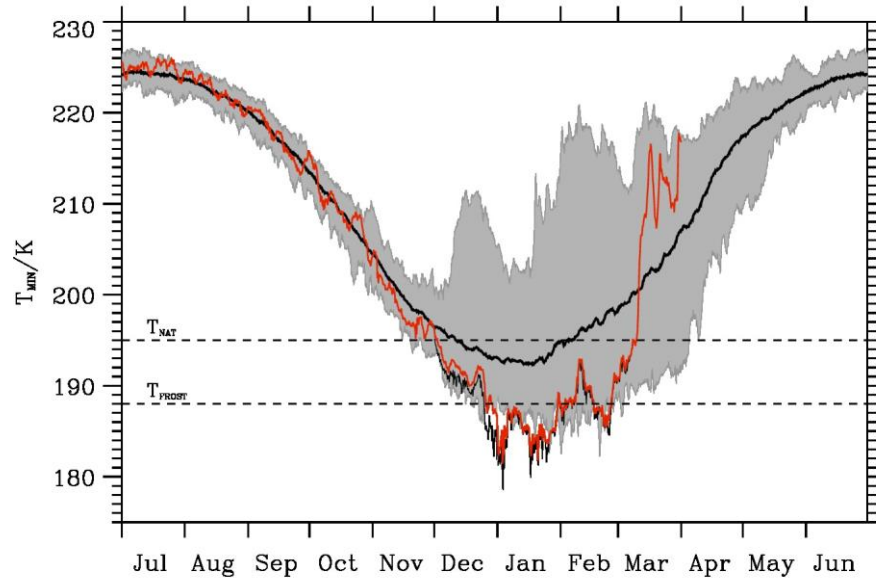
481 **Figure 1:** Composite of 532 nm total attenuated backscatter ($10^{-3} \text{ km}^{-1} \text{ sr}^{-1}$, color shaded) from CALIOP
 482 and ECMWF potential temperature (top, K, solid black lines) and absolute temperature (bottom, K, thin
 483 black lines every 5 K and thick black lines at 185 K and 191 K) valid on 30 December 2015 at 04 UTC (+
 484 4 h lead time from the 00 UTC HRES IFS forecast of cycle 41r2.

485
486
487
488
489
490
491
492
493
494



495
496
497
498

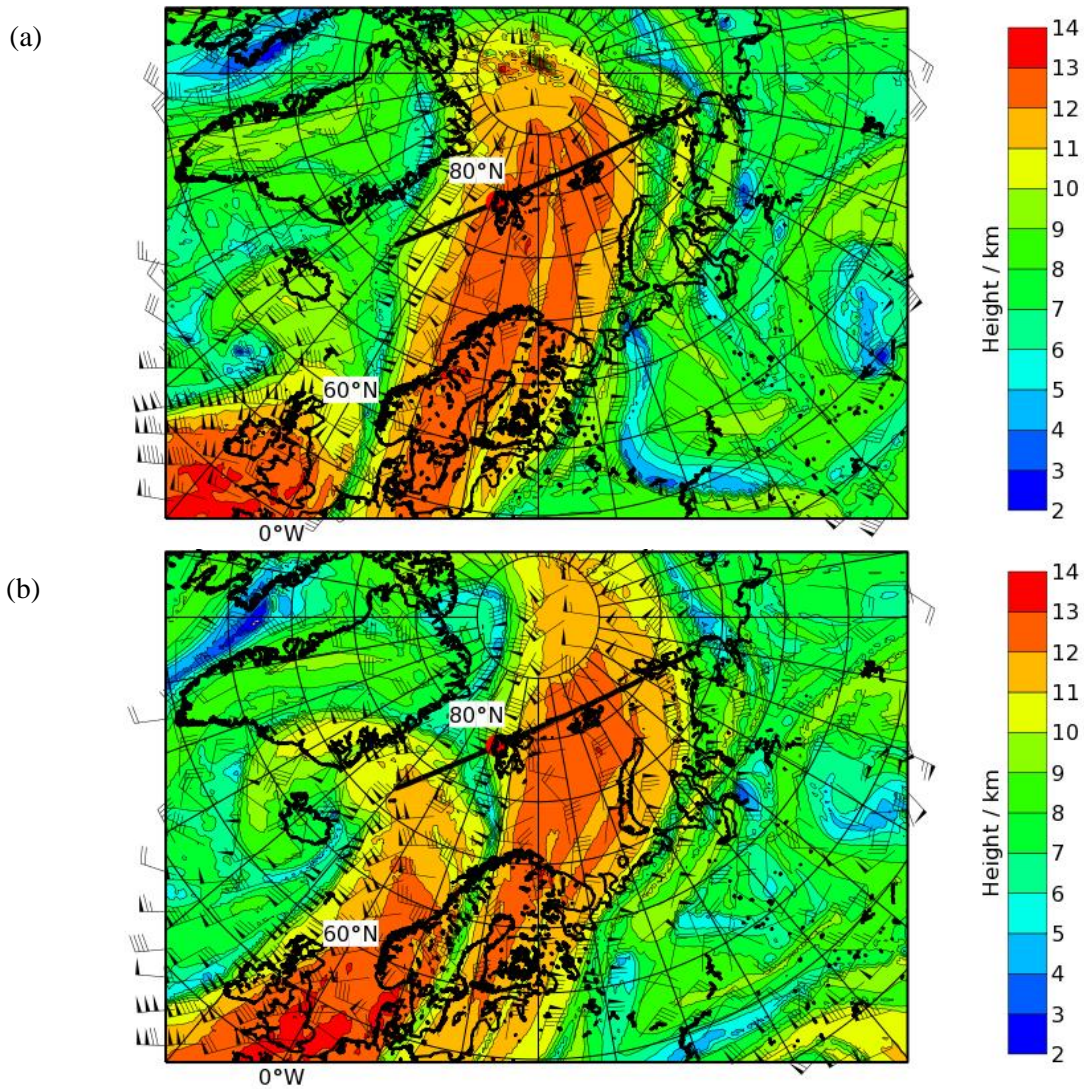
Figure 2: Thermal infra-red image (NOAA 19, channel 4: 10.3-11.3 μ m) on 30 December 2015 0440 UTC with the first third of the path of the CALIOP measurements (Fig. 1) as black arrow. Image provided by NERC Satellite Receiving Station, Dundee University, Scotland (<http://www.sat.dundee.ac.uk>).



499

500 **Figure 3:** 6 hourly ECMWF reanalyses interim (ERA-Interim, Dee et al., 2011) data retrieved at a
 501 horizontal resolution of 1° : Minimum temperature T_{MIN} (K) between 65°N to 90°N at the 50 hPa pressure
 502 surface. Thick black line denotes the mean values of T_{MIN} averaged from 1979 – 2015, the shaded areas
 503 encompass the minimum and maximum values of T_{MIN} attained at every date between 1979 and 2015.
 504 The red line marks the evolution of T_{MIN} from operational analyses of the IFS cycle 41r1 until 8 March
 505 2016. The thin black line indicates T_{MIN} from the IFS cycle 41r2 in the pre-operational phase 1 December
 506 2015 until 8 March 2016 retrieved at a resolution of 0.125° . After 8 March 2016, the black line continues
 507 as red curve of the operational IFS cycle 41r2.

508

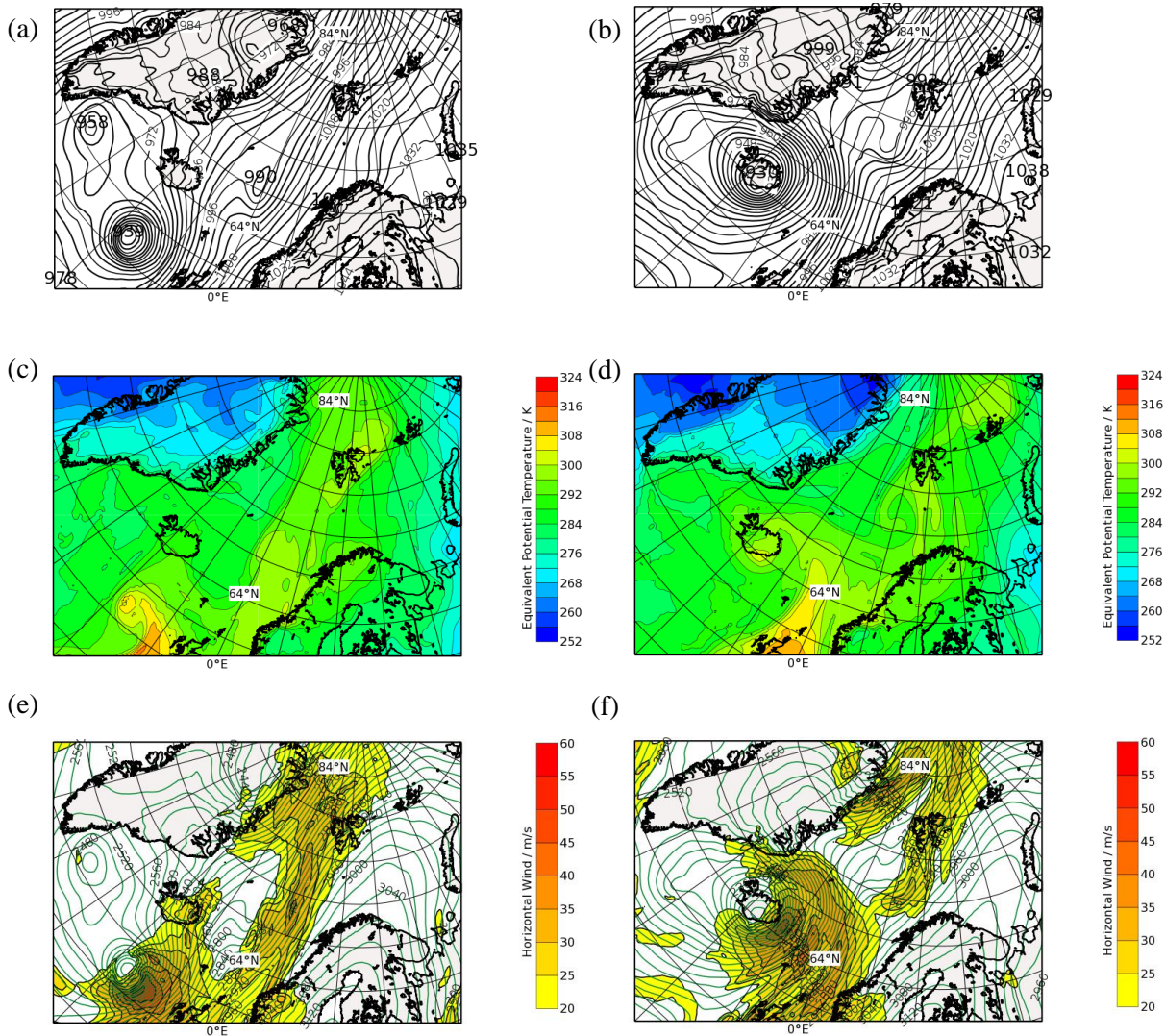


509

510

511 **Figure 4:** Height of the dynamical tropopause (km, color shaded) and horizontal wind (m s^{-1} , barbs) at the
 512 2 PVU surface on 29 December 2015 18 UTC (a) and 30 December 2015 06 UTC (b). The path of the
 513 CALIPSO overpass is plotted as solid black line, the location of Ny-Ålesund, Svalbard is marked by a red
 514 dot.

515



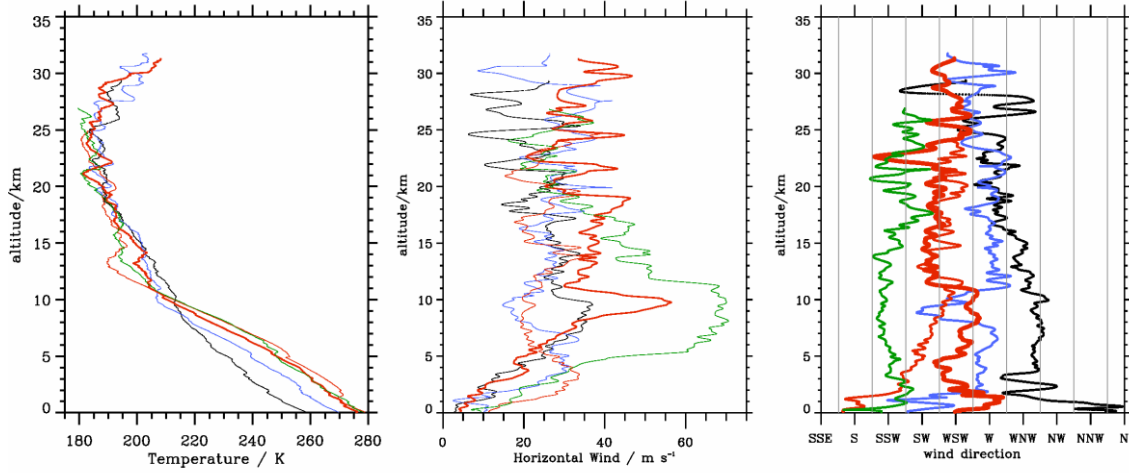
516

517

518

519 **Figure 5:** Tropospheric charts valid on 29 December 2015 18 UTC (left column) and
 520 06 UTC (right column). (a,b): Mean sea level pressure (hPa, contour lines), (c,d): Equivalent potential
 521 temperature (K, color shaded) at 850 hPa, and (e,f): horizontal wind (m s^{-1} , color shaded) and geopotential
 522 height (m, contour lines) at 700 hPa.

523



524

525 **Figure 6:** Vertical profiles of absolute temperature (a), horizontal wind (b), and wind direction (c) from
526 radiosonde launches in Ny-Ålesund, Svalbard on 27 December (black), 28 December (blue), 29 December
527 (thin red), 30 December (thick red), and 31 December (green) 2015 12 UTC, respectively.

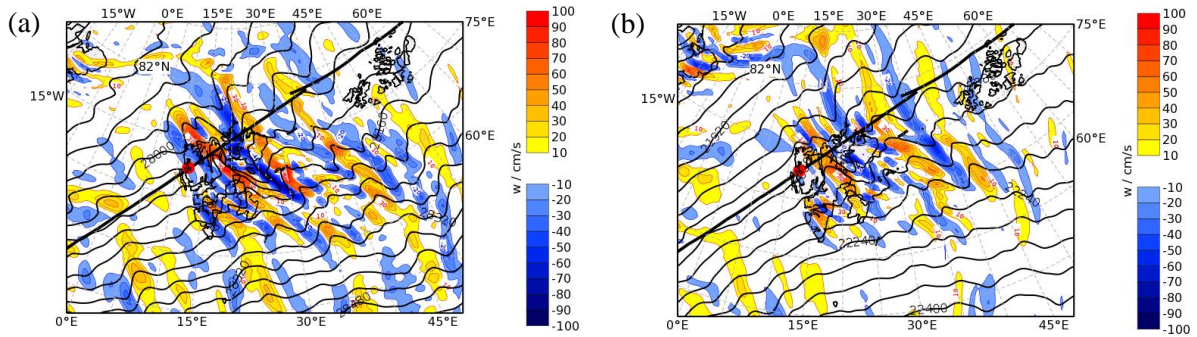
528

529

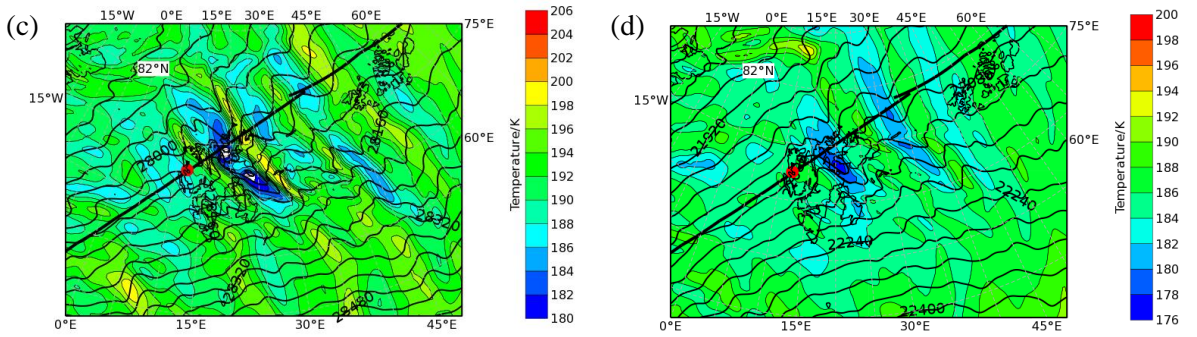
530

531

532

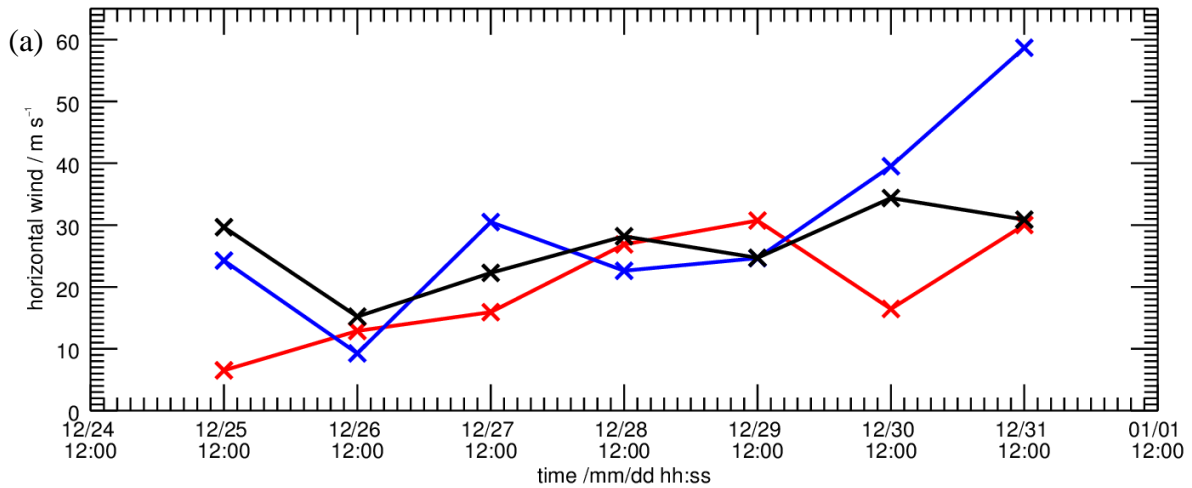


533

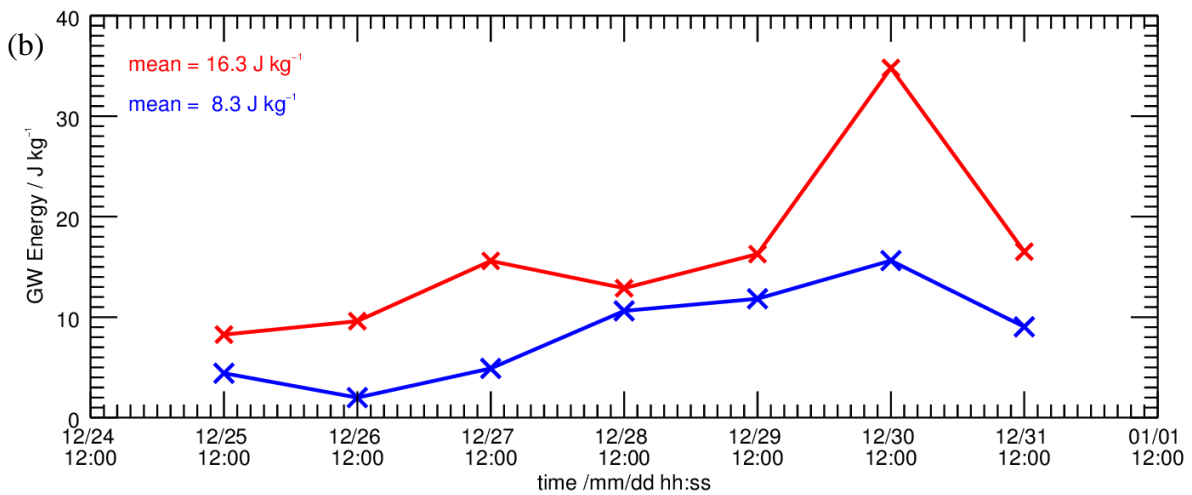


534

535 **Figure 7:** Vertical velocity (m s^{-1} , color shading, top row), absolute temperature (K, color shading, bottom
536 row), and geopotential height (m, black contour lines) from the IFS cycle 41r2 at 10 hPa (a, c) and at 30
537 hPa (b,d) valid on 30 December 2015 06 UTC. The path of the CALIPSO overpass is plotted as solid
538 black line, the location of Ny-Ålesund, Svalbard is marked by a red dot.



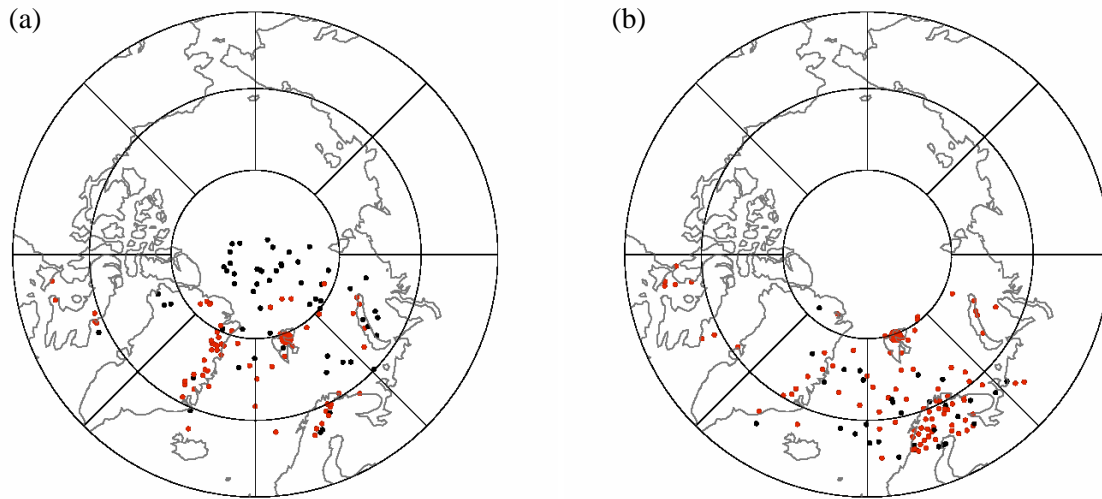
539



540

541 **Figure 8:** (a) Vertically averaged horizontal wind in the lower troposphere (2 to 5 km, red crosses), the
 542 tropopause region (8 to 15 km, blue crosses), and in the stratosphere (15 to 25 km, black crosses). (b)
 543 Stratospheric gravity wave kinetic and potential energies (red and blue crosses, respectively) determined
 544 from the radiosonde soundings of Ny-Ålesund, Svalbard in an altitude range of 15 to 25 km.

545



546

547 **Figure 9:** Locations of the polar cap minimum temperatures T_{MIN} at 30 hPa (a) and 50 hPa (b) from 6
 548 hourly ECMWF IFS cycle 41r2 analyses for December 2015. The red dots mark T_{MIN} -values where the
 549 absolute value of the horizontal divergence is larger than $2 \cdot 10^{-4} \text{ s}^{-1}$. The large symbol is the location of
 550 T_{MIN} on 30 December 2015 at 06 UTC.